A New Method for Processing the Forward Solver Data in Fluorescence Molecular Imaging

Dimitris Gorpas, Kostas Politopoulos, and Dido Yova

***Abstract*—During the last few years a quite large number of fluorescence imaging applications have been reported in the literature, as one of the most challenging problems in medical imaging is to "see" a tumour embedded in tissue, which is a turbid medium. This problem has not been fully encountered yet, due to the non-linear nature of the inverse problem. In this paper, a novel method for processing the forward solver outcomes is presented. Through this technique the comparison between the simulated and the acquired data can be performed only at the region of interest, minimizing time-consuming pixel-to-pixel comparison. With this modus operandi a-priory information about the initial fluorophore distribution becomes available, leading to a more feasible inverse problem solution.**

I. Introduction

THE combined progress in fluorescent probes technology and optical imaging modalities have encountered a number of difficulties in the noise dominated fluorescence image acquisition. Nevertheless, fluorescence signal processing still lacks the feasibility and time efficacy, due to the enormous amount of the recorded data. The current state-of-the-art in fluorescence molecular imaging applications requires parallel programming with multiple computational units and computational time in the order of hours. The most important reason for this lack of time efficacy is the non-linear nature of the inverse problem, which requires iterative procedures for convergence [1], and the pixel-to-pixel comparison between measured and computed data [2].

In this paper, a novel method for processing the forward solver outcomes is presented. Through this technique the comparison between the simulated and the acquired data can be performed only at the region of interest, minimizing time-consuming pixel-to-pixel comparison.

Within this work a custom forward solver has been developed, based on the Diffusion Approximation [3]. Galerkin finite elements [4] have been introduced to originate the variational formulation of the Diffusion Approximation, whereas a Delaunay triangulation scheme [5] has been applied for the region discretization. For the three-dimensional simulation of the fluorophores distribution, the super-ellipsoid models [6] have been selected. Those models have been extensively used in various machine vision applications [7], [8], however this is the first time these are used to simulate fluorophore distribution in a fluorescence molecular imaging application.

The estimated fluorescence emission distribution over the region surface is converted into intensity levels, which corresponds to the measurand of the imaging system [9]. However, a back-projection scheme is required to transform the global coordinates of the simulated signal into image local coordinates, and eventually pixels. This back-projection requires accurate knowledge of the imaging system calibration parameters, which are the relation (translation and rotation) between the global coordinates system and the camera-centered system and the distortion parameters that the camera lens adds. Furthermore, the filter transmission factor should be incorporated into the simulated signal, in order to match the real acquisition system [9].

Once the simulated image has been formulated, image segmentation algorithms are applied, in order to perform an accurate segmentation. Morphological filtering provides a contrast enhancement, whereas a custom watershed transformation [10] extracts the region of interest from the simulated image. It is essential that the same algorithms will be applied to the acquired images as well, since intensity levels, along with the geometrical features, would lead to the image registration convergence.

II. Methodology

A. Forward Solver

In the Diffusion Approximation the Radiative Transfer Equation can be expressed by the P_1 approximation [11]:

$$(i\omega/c)U(\mathbf{r}) = \nabla\left[D(\mathbf{r})\nabla U(\mathbf{r})\right] - \mu_a(\mathbf{r})U(\mathbf{r}) + \Lambda_0(\mathbf{r}) \qquad (1)$$

where ω is the angular modulation frequency of the light source in sr/s, c is the average speed of light in the medium with typical value in the case of tissue $c = 2.55 \cdot 10^{10}$ cm/s,

Manuscript received June 14, 2008. This work was supported by the European Committee under the Integrated Project "World Wide Welfare: high BRIGHTnes semiconductor lasERs for gEneric Use", IST-2005-2.5.1 Phot.

D. Gorpas is with the Laboratory of Biomedical Optics and Applied Biophysics, School of Electrical and Computer Engineering, National Technical University of Athens, GR-157 73, Zografou, Greece (phone: +302107722293; fax: +302107723048; e-mail: dgorpas@ mail.ntua.gr).

K. Politopoulos is with the Laboratory of Biomedical Optics and Applied Biophysics, School of Electrical and Computer Engineering, National Technical University of Athens, GR-157 73, Zografou, Greece (e-mail: policent@central.ntua.gr).

D. Yova is with the Laboratory of Biomedical Optics and Applied Biophysics, School of Electrical and Computer Engineering, National Technical University of Athens, GR-157 73, Zografou, Greece (e-mail: didoy@central.ntua.gr).

$U(\mathbf{r})$ is the average intensity or fluence in W/cm^2, $D(\mathbf{r})$ is the photon diffusion coefficient in cm, $\mu_a(\mathbf{r})$ is the medium absorption coefficient in cm^{-1} and $\Lambda_0(\mathbf{r})$ is the isotropic component of the source in W/cm^2. The photon diffusion coefficient is expressed as:

$$D(\mathbf{r}) = (1/3)\left[a\mu_a(\mathbf{r}) + \mu_s'(\mathbf{r})\right]^{-1} \tag{2}$$

with $\mu_s'(\mathbf{r})$ being the reduced scattering coefficient in cm^{-1}, whereas the factor a is related to the absorption, scattering and anisotropy of the medium. In the case of tissue, this factor is in the order of $a \sim 0.5$, assuming anisotropy $g \sim 0.8$ [12].

The exact boundary condition for the diffuse intensity requires that there should be no diffuse intensity re-entering the medium from outside, at the surface S. However, this boundary condition cannot be satisfied exactly and some approximate boundary conditions must be considered. One such approximation requires that the total diffuse flux detected inwards at the surface S should be zero [3]. This condition in terms of the average intensity $U(\mathbf{r})$, taking into account the mismatch between the refractive indices of the inspected medium and the surrounding one, is expressed by the Robin type condition [11] [13] as:

$$U(\mathbf{r}) = -2RD(\mathbf{r})\left[\partial U(\mathbf{r})/\partial\bar{\mathbf{n}}\right] \quad \mathbf{r}\in S,\ \bar{\mathbf{s}}\cdot\bar{\mathbf{n}} < 0 \tag{3}$$

where the coefficient R represents the boundary reflection coefficient and depends on the mismatch between the refraction indices. For a typical tissue/air value of relative index of refraction of tissue with respect to air, $n_{tis/air} = 1.33$, this coefficient equals to $R = 2.34$ [12].

In fluorescence imaging two light fields are taken into consideration, the excitation and the emission. For the excitation light, indexed *exc*, the only light source is the external excitation light $I_{src}(\mathbf{r})$. On the other hand, for the emission field, indexed *em*, there exist only the internal fluorescence sources. Thus assuming fluorophore quantum yield η, the internal light sources are described as:

$$\Lambda_{em}(\mathbf{r}) = \eta\mu_{a,exc}^{fluo}(\mathbf{r})\left[1 - i\omega\tau(\mathbf{r})\right]^{-1}U_{exc}(\mathbf{r}) \tag{4}$$

where $\mu_{a,exc}^{fluo}(\mathbf{r})$ is the absorption coefficient of the fluorophores at the excitation wavelength, $\tau(\mathbf{r})$ is the fluorophore lifetime in s and $U_{exc}(\mathbf{r})$ is the average intensity of the excitation light.

Under these premises and taking into consideration (1) and (3) the following equation system arises:

$$\left[(i\omega/c) + \mu_{a,exc}(\mathbf{r})\right]U_{exc}(\mathbf{r}) - \nabla\left[D_{exc}(\mathbf{r})\nabla U_{exc}(\mathbf{r})\right] = 0 \tag{5}$$

$$\left[(i\omega/c) + \mu_{a,em}(\mathbf{r})\right]U_{em}(\mathbf{r}) - \nabla\left[D_{em}(\mathbf{r})\nabla U_{em}(\mathbf{r})\right] = \eta\mu_{a,exc}^{fluo}(\mathbf{r})\left[1 - i\omega\tau(\mathbf{r})\right]^{-1}U_{exc}(\mathbf{r}) \tag{6}$$

$$U_{exc}(\mathbf{r}) + 2RD_{exc}(\mathbf{r})\left[\partial U_{exc}(\mathbf{r})/\partial\bar{\mathbf{n}}\right] = 4I_{src}(\mathbf{r}) \tag{7}$$

$$U_{em}(\mathbf{r}) + 2RD_{em}(\mathbf{r})\left[\partial U_{em}(\mathbf{r})/\partial\bar{\mathbf{n}}\right] = 0 \tag{8}$$

Within this model it is assumed that the presence of the fluorophores does not alter the reduced scattering coefficient of the tissue. However, the absorption coefficient is assumed to be the sum of tissue absorption coefficient and the one of the fluorophores, $\mu_{a,exc/em}(\mathbf{r}) = \mu_{a,exc/em}^{tis}(\mathbf{r}) + \mu_{a,exc/em}^{fluo}(\mathbf{r})$.

A finite elements solution of the Diffusion Approximation model can be derived by posing the model in a weak variational form with the use of piecewise linear functions [14]. To obtain the variational formulation of the model it is taken into consideration the fact that the solution of (5), is the light source for (6). Thus, the two equations will be confronted separately, to prevent the occurrence of unstable equation systems.

Therefore, the excitation field (5) is multiplied with the test function $\psi(\mathbf{r})$ and integrated over the domain V:

$$(i\omega/c)\int_V U_{exc}(\mathbf{r})\psi(\mathbf{r})dr + \int_V \mu_{a,exc}(\mathbf{r})U_{exc}(\mathbf{r})\psi(\mathbf{r})dr - \int_V \nabla\left[D_{exc}(\mathbf{r})\nabla U_{exc}(\mathbf{r})\right]\psi(\mathbf{r})dr = 0 \tag{9}$$

Using the first Green's identity, an extension to the theorem of divergence for integration by parts [15], it is obtained:

$$\int_V \nabla\left[D_{exc}(\mathbf{r})\nabla U_{exc}(\mathbf{r})\right]\psi(\mathbf{r})dr = \int_S D_{exc}(\mathbf{r})\left[\bar{\mathbf{n}}\nabla U_{exc}(\mathbf{r})\right]\psi(\mathbf{r})dr - \int_V D_{exc}(\mathbf{r})\nabla U_{exc}(\mathbf{r})\nabla\psi(\mathbf{r}) \tag{10}$$

The boundary integral term in (10) can be written as:

$$\int_S D_{exc}(\mathbf{r})\left[\bar{\mathbf{n}}\nabla U_{exc}(\mathbf{r})\right]\psi(\mathbf{r})dr = 2R^{-1}\int_{S_{src}} I_{src}(\mathbf{r})\psi(\mathbf{r})dr - (2R)^{-1}\int_S U_{exc}(\mathbf{r})\psi(\mathbf{r})dr \tag{11}$$

where the Robin type boundary condition of (7) was taken into consideration. Inserting (10) and (11) into (9), the required variational (weak) formulation is obtained:

$$(i\omega/c)\int_V U_{exc}(\mathbf{r})\psi(\mathbf{r})dr + \int_V D_{exc}(\mathbf{r})\nabla U_{exc}(\mathbf{r})\nabla\psi(\mathbf{r}) + (2R)^{-1}\int_S U_{exc}(\mathbf{r})\psi(\mathbf{r})dr + \int_V \mu_{a,exc}(\mathbf{r})U_{exc}(\mathbf{r})\psi(\mathbf{r})dr = (R/2)\int_{S_{src}} I_{src}(\mathbf{r})\psi(\mathbf{r})dr \quad (12)$$

In order to obtain the finite element approximation of the Diffusion Approximation model, the solution $U_{exc}(\mathbf{r})$ of the variational formulation (12) is approximated in piecewise linear functions per element, based on the nodal values of the $U_{exc}(\mathbf{r})$ solution. Hence, the discretization of $U_{exc}(\mathbf{r})$, following the Galerkin method [4] [15] is expressed as:

$$U_{exc}(\mathbf{r}) \approx U^h_{exc}(\mathbf{r}) = \sum_{k=1}^{N} a_{k,exc}\psi_k(\mathbf{r}) \quad (13)$$

where $\psi_k(\mathbf{r})$ are the nodal basis functions of the finite elements discretization, $a_{k,exc}$ is the photon density in nodal point k, with $k = 1,\mathsf{L}\ ,N$, and N is the number of nodal points. Furthermore, as test functions the test functions $\psi_p(\mathbf{r})$, $p = 1,\mathsf{L}\ ,N$, are chosen, in order to obtain the algebraic equations for all the unknowns. The resulting system is linear algebraic, expressed in matrix mode as:

$$\mathbf{A}_{exc}\mathbf{a}_{exc} = \mathbf{f}_{exc} \quad (14)$$

where $\mathbf{a}_{exc} = \left[a_{k,exc}\right]$ is the photon density of the excitation field in nodal points of the finite element mesh. The matrix $\mathbf{A}_{exc}$ contains the finite element approximation of the Diffusion Approximation model and it is of the form:

$$\mathbf{A}_{exc}(p,k) = \mathbf{Ke}_{exc}(p,k) + \mathbf{Me}_{exc}(p,k) + \mathbf{Pe}_{exc}(p,k) \quad (15)$$

with $\mathbf{Ke}_{exc}(p,k)$ being the mass matrix, $\mathbf{Me}_{exc}(p,k)$ being the stiffness matrix and $\mathbf{Pe}_{exc}(p,k)$ being the boundary condition matrix of the finite element approximation:

$$\mathbf{Ke}_{exc}(p,k) = (i\omega/c)\int_V \psi_k(\mathbf{r})\psi_p(\mathbf{r})dr + \int_V \mu_{a,exc}(\mathbf{r})\psi_k(\mathbf{r})\psi_p(\mathbf{r})dr \quad (16)$$

$$\mathbf{Me}_{exc}(p,k) = \int_V D_{exc}(\mathbf{r})\nabla\psi_k(\mathbf{r})\nabla\psi_p(\mathbf{r})dr \quad (17)$$

$$\mathbf{Pe}_{exc}(p.k) = (2R)^{-1}\int_S \psi_k(\mathbf{r})\psi_p(\mathbf{r})dr \quad (18)$$

Under the same modus operandi, a similar matrix system derives for the emission field, as described in (6). All the matrices for this field are approximated as in the excitation case. Moreover, the source vector is of the form:

$$\mathbf{f}_{em}(p) = \mathbf{c}(p,k)\mathbf{a}_{exc}(k) \quad (19)$$

with the matrix $\mathbf{c}(p,k)$ being as follows:

$$\mathbf{c}(p,k) = \eta\int_V \mu^{fluo}_{a,exc}(\mathbf{r})\left[1 - i\omega\tau(\mathbf{r})\right]^{-1}\psi_k(\mathbf{r})\psi_p(\mathbf{r})dr \quad (20)$$

Thus from (19) the coupling between the excitation and the emission models becomes apparent. However, in order to avoid any unstable conditions, due to matrix inversions and multiplications, the problem confrontation is succeeded separately for each model. Furthermore, it becomes obvious that the finite elements discretization scheme must be the same between the two models; otherwise the excitation model solution should be updated to the new discretization, resulting into accuracy losses and decrease of time efficacy.

B. Region Discretization

The region under inspection was discretized via application of the Delaunay triangulation scheme [5]. Delaunay triangulation is a pure geometrical discretization technique and it is among the most common techniques applied to Finite Elements problems. The elements that have been selected for the described forward solver were linear tetrahedral elements, distributed over a uniform mesh. The set of tetrahedral coordinates ζ_1, ζ_2, ζ_3 and ζ_4 are in terms of a parametric coordinate system and in literature they receive different names, such as isoparametric coordinates or shape function coordinates.

The geometric definition of the element in terms of these coordinates is expressed as:

$$\begin{bmatrix}\zeta_1\\ \zeta_2\\ \zeta_3\\ \zeta_4\end{bmatrix} = \frac{1}{6V}\begin{bmatrix}a_1 & b_1 & c_1 & d_1\\ a_2 & b_2 & c_2 & d_2\\ a_3 & b_3 & c_3 & d_3\\ a_4 & b_4 & c_4 & d_4\end{bmatrix}\cdot\begin{bmatrix}1\\ x\\ y\\ z\end{bmatrix} \quad (21)$$

where the sixteen matrix entries depend only on the vertex locations of the tetrahedron and V is the elemental volume.

Utilizing these elemental definitions, the mass and stiffness matrices can be approximated by expressing them in the simplex coordinates [15].

The fluorophore distribution was simulated by applying the super-ellipsoid model, defined as the solution of the general form of the implicit equation:

$$f(x,y,z) = \left[\left(x/\alpha_1\right)^{2/\varepsilon_2} + \left(y/\alpha_2\right)^{2/\varepsilon_2}\right]^{\varepsilon_2/\varepsilon_1} + \left(z/\alpha_3\right)^{2/\varepsilon_1} \quad (22)$$

In this equation, one can recognize an ellipsoid form, enriched by two more parameters, ε_1 and ε_2, that allow

controlling the shape curvature. As for the ellipsoid case, the α_1, α_2 and α_3 parameters are scale factors on x, y and z axis respectively, Fig. 1.

The form of (22) gives information on the position of a three-dimensional point, related to the super-ellipsoid surface, which is critical for interior/exterior determination. This information derives from the following critical values of the implicit equation: $f(x,y,z)=1$ when the point lies on the surface, $f(x,y,z)<1$ when the point is inside the super-ellipsoid and $f(x,y,z)>1$ when it is outside of the super-ellipsoid. In the case of fluorophore distribution, the absorption coefficient can be expressed, utilizing these values, as:

$$\mu_a(\mathbf{r})=\mu_a^{tis}(\mathbf{r})+c\mu_a^{fluo}(\mathbf{r}),\quad c=\begin{cases}1, & f(x,y,z)\le 1\\ 0, & f(x,y,z)>1\end{cases} \tag{23}$$

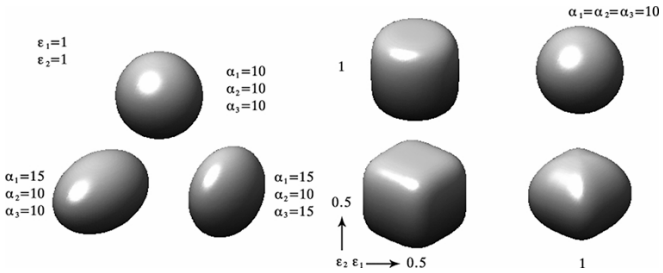

Fig. 1. Super-ellipsoid models for various parameters values

C. Image Formulation

The formulation of the images, after the solution of the forward problem, in the case of the Diffusion Approximation was based on the following expression:

$$X(\mathbf{r})=U_{em}(\mathbf{r})/(2R) \tag{24}$$

where $X(\mathbf{r})$ is the measurable quantity. Within this formulation, losses in the imaging system are taken into consideration and accounted as a correlation factor. This factor is experimentally calculated through the system calibration procedure [9] [16].

Camera calibration is the process of determining the internal camera geometric and optical characteristics (intrinsic parameters) and/or the three-dimensional position and orientation of the camera frame relative to a certain world coordinate system (extrinsic parameters) [17].

The most important premise for an accurate calibration is the correct mathematical expression of the camera model. Assuming telecentric lenses, the pinhole camera model [18] is not applicable. Telecentric lenses perform orthographic projection and are ideal for gauging applications, thus the projection of an arbitrary point (X_i,Y_i,Z_i) to the image plane is expressed as:

$$\begin{bmatrix}u_i'\\ v_i'\\ 1\end{bmatrix}=\begin{bmatrix}a_u & s & 0 & 0\\ 0 & a_v & 0 & 0\\ 0 & 0 & 0 & 1\end{bmatrix}\cdot\begin{bmatrix}r_{11} & r_{12} & r_{13} & x_0\\ r_{21} & r_{22} & r_{23} & y_0\\ r_{31} & r_{32} & r_{33} & z_0\\ 0 & 0 & 0 & 1\end{bmatrix}\cdot\begin{bmatrix}X_i\\ Y_i\\ Z_i\\ 1\end{bmatrix} \tag{25}$$

where the coefficients a_u, a_v and s are scale factors for transforming the image plane metric units $(\bar{u}_i,\bar{v}_i)$ to image pixels (u_i',v_i') and represent the camera intrinsic parameters. $\mathbf{R}=[r_{ij}]$ is the rotation matrix and $\mathbf{T}=[x_0 \quad y_0 \quad z_0]^T$ is the translation matrix. These two matrices define the extrinsic parameters of the camera frame. Finally (X_i,Y_i,Z_i) are the global coordinates of the arbitrary point.

Although telecentric lenses optically compensate for lens distortions, there should be taken into account at least the most common types of distortion, to avoid any possible lens construction errors [19]. The overall distortion equation is:

$$\begin{bmatrix}\delta u_i\\ \delta v_i\end{bmatrix}=\begin{bmatrix}\bar{u}_i r_i^2 & \bar{u}_i r_i^4 & 2\bar{u}_i\bar{v}_i & r_i^2+2\bar{u}_i^2\\ \bar{v}_i r_i^2 & \bar{v}_i r_i^4 & r_i^2+2\bar{v}_i^2 & 2\bar{u}_i\bar{v}_i\end{bmatrix}\cdot\begin{bmatrix}k_1\\ k_2\\ p_1\\ p_2\end{bmatrix} \tag{26}$$

where (k_1,k_2) are the radial distortion parameters, (p_1,p_2) are the tangential distortion coefficients and $r_i^2=\bar{u}_i^2+\bar{v}_i^2$.

Having experimentally solved the calibration problem for these parameters, the mapping between the global coordinates system to the image plane is possible, which means that the $X(\mathbf{r})$ in (24) can now be expressed as $X(u,v)$. Furthermore, the fluence values are thresholded by the fluorescence filters transmission factor Q_E. Finally, the virtual image formulation is expressed as:

$$X(\mathbf{r})=Q_E U(\mathbf{r})/(2R)\rightarrow X(u,v) \tag{27}$$

D. Image Segmentation

The simulated image for each measurement is pre-processed and normalized, in order to meet the acquisition protocol. The pre-processing algorithms include intensity adjustment and contrast enhancement. The intensity adjustment was performed by mapping the intensity values of each image to new ones, between 0 (black) and 1 (white). Values below the low and above the high thresholds are clipped; that is values below the low threshold mapped to 0 and those above the high threshold mapped to 1. Extensive testing revealed that the most appropriate mapping was the one that was weighted toward lower (darker) output values.

An expected side effect of the intensity adjustment is the weakening of the region-of-interest edges. However, the described algorithm overcame this difficulty via morphological image processing. More specific, opening

filter can produce a reasonable estimate of the background across the image, as long as the selected structuring element is large enough not to fit entirely within any of the objects of interest. Subtracting the resulted image from the restored, a new one with even background arises (top-hat transformation). Repeating the same procedure, but instead of opening applying the closing filter (bottom-hat transformation), and multiplying the outcomes, a contrast enhancement was succeeded.

After the preprocessing procedure the image is ready for the segmentation. Simple thresholding would lead either to the exclusion of some features or to the region growth of others. On the other hand, application of any edge detection or segmentation algorithm would lead to falsely detected edges or over-segmentation. The reason is that the object in the images does not have sharp edges or relevant intensities. In order to avoid such problems, this algorithm performed a combination of marker-controlled watershed transformation and thresholding. As a result even the lowest intensity features were detected.

Through this procedure, the region-of-interest from the simulated images was extracted. This will be the input to the image registration problem, where the matching between the acquired and the simulated data is evaluated. However, this matching process does not seek the entire images, but only the regions of interest, minimizing significantly the timing required to solve the inverse problem.

III. Results

The synthetic frequency-domain fluorescence data were generated on a simulated 2 cm × 2 cm × 2 cm cube, with its center located at the origin of the coordinates system, illuminated by a simulated point laser beam with a Dirac profile at the $z=1$ plane and angular modulation frequency $\omega = 100$ MHz. The refractive mismatch at the boundary of the region was set at $R = 2.34$ and the average speed of light in the medium at $c = 2.55 \cdot 10^{10}$ cm/s.

Data were generated for two different super-ellipsoid models at two different locations. The first super-ellipsoid model was a sphere with diameter $r = 0.25$ cm and the second model was an ellipsoid with x-axis diameter 0.125 cm, y-axis diameter 0.25 cm and z-axis diameter 0.125 cm. These two models were firstly located at the origin of the coordinates system, while their second location was off-axis with their center located at the point $(0.25, 0.25, 0.5)$.

For the simulated absorption coefficient were chosen the values $\mu_{a,exc}^{tis} = 0.023$ cm^{-1} and $\mu_{a,em}^{tis} = 0.0289$ cm^{-1} for the background and $\mu_{a,exc}^{fluo} = 0.5$ cm^{-1} and $\mu_{a,em}^{fluo} = 0.0506$ cm^{-1} for the fluorophore. The lifetime of the fluorophore was taken to be $\tau = 0.56 \cdot 10^{-9}$ s independent from the position and the quantum efficiency was $\eta = 0.016$, to match the corresponding properties of the Indocyanine Green (ICG) dye, commonly used in experiments. Finally, the reduced scattering coefficient was taken as $\mu_s' = 9.84$ cm^{-1} in both the target and the background, and was considered to be constant for both excitation and emission wavelengths.

The region was discretized at 24576 uniformly distributed linear tetrahedral elements, which means a number of 4913 nodal points. The simulations were performed at a 2.16 GHz Dual Core unit with 2 GB RAM and required approximately 30 minutes for the forward solver to converge to a solution. In Fig. 2 the outcomes of the forward solver for the four cases of simulation measurements are presented as sliced surfaces at the $z=1$ plane.

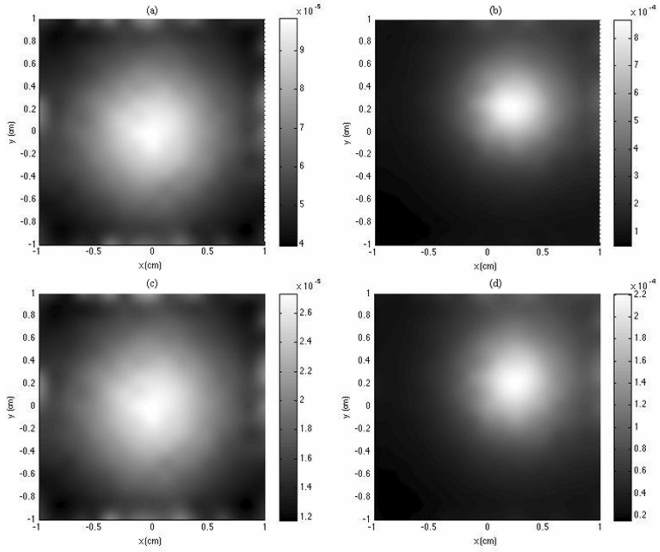

Fig. 2. Surface slices presenting the fluence exiting the cube for the four cases of super-ellipsoid models. (a) and (b) show the spherical model located at the center of the cube (a) and off-axis (b). (c) and (d) present the ellipsoid model for the same locations respectively.

By application of (27) the slices of Fig. 2 are transformed to image data and presented in Fig. 3. The calibration parameters that were used for this transformation have chosen to correspond to an 800×800 pixels camera, with the use of telecentric lens. The fluorescence filters transmission factor was set at $Q_E = 0.9$, to correspond to most high-end commercial fluorescence filters at the emission wavelength of the ICG.

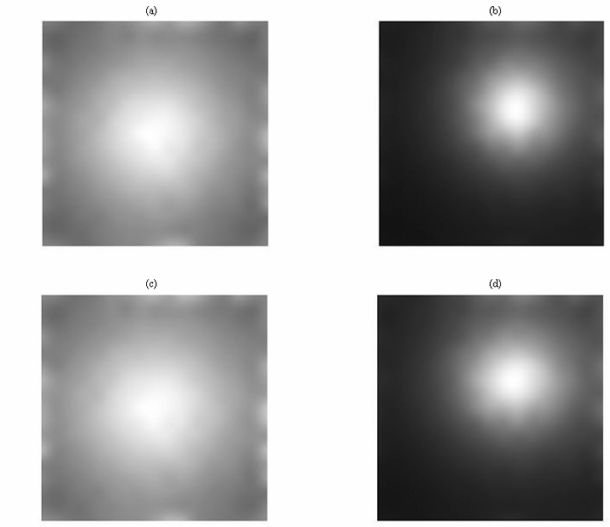

Fig. 3. Images after application of the fluence transformation. (a) and (b) show the spherical model located at the center of the cube (a) and off-axis (b). (c) and (d) present the ellipsoid model for the same locations respectively.

Fig. 4 shows the restored images after the preprocessing algorithms. The difference between Fig. 3 and Fig. 4 is obvious. The region-of-interest in Fig. 4 is well determined and the contrast enhancement presents high levels.

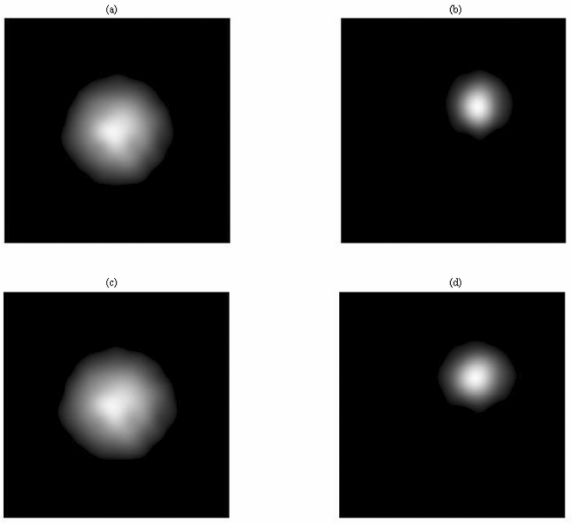

Fig. 4. Restored images after application of the preprocessing algorithms. (a) and (b) show the spherical model located at the center of the cube (a) and off-axis (b). (c) and (d) present the ellipsoid model for the same locations respectively.

Finally, in Fig. 5 the segmented images are presented. Comparing Fig. 4 and Fig. 5 one can notice the accurate segmentation that the custom watershed transformation has achieved.

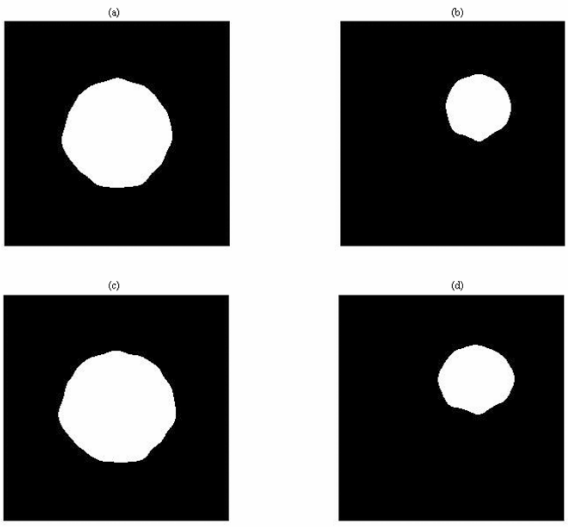

Fig. 5. Segmented images (a) and (b) show the spherical model located at the center of the cube (a) and off-axis (b). (c) and (d) present the ellipsoid model for the same locations respectively.

Through this point the extraction of the intensity histogram and the geometrical properties of the region-of-interest is possible, which will conclude to a more feasible comparison between real and simulated images.

IV. Conclusion

In this paper a new method for the processing of the forward solver outcomes in fluorescence molecular imaging has been presented. This method is based on computer vision algorithms and succeeds to isolate the region-of-interest from the noisy background, a very important aspect for the convergence of the inverse problem.

Another important aspect of this work is the introduction of the super-ellipsoids as the simulation models. With only eleven parameters, an excessively large number of tumour simulations can result automatically and the required initial values of the fluorophore distribution to be available. This is of great importance as the lack of these values is mostly responsible for the time consuming iterations during the solution of the inverse problem.

References

[1] V. Ntziachristos, "Fluorescence Molecular Imaging," *Annu. Rev. Biomed. Eng.*, vol. 8, pp. 1-33, 2006.

[2] A. Joshi, W. Bangerth, E.M. Sevick-Muraca, "Adaptive finite elements based tomography for fluorescence optical imaging in tissue," *Opt. Express*, vol. 12, pp. 5402-5417, 2004.

[3] A. Ishimaru, "Wave Propagation and Scattering in Random Media," *Vol 1: Single Scattering and Transport Theory*, Academic Press, New York, 1978.

[4] T.K. Sengupta, S.B. Talla, S.C. Pradhana, "Galerkin finite element methods for wave problems," *Sadhana*, vol. 30, pp. 611-623, 2005.

[5] P.L. George, H. Borouchaki, "Delaunay Triangulation and Meshing," *Hermes*, Paris, 1998.

[6] Y. Fougerolle, A. Gribok, S. Foufou, F. Truchetet, M. Abidi, "Implicit Surface Modeling using Supershapes and R-functions," *In Proc. of Pacific Graphics '05*, Macao, China, pp. 169-172, 2005.

[7] L. Chevalier, F. Jaillet, A. Baskurt, “Segmentation and superquadric modeling of 3D objects,” *In Proceedings of WSCG 2003*, Plzen, Czech Republic, 2003.

[8] J.A. Tyrrell, B. Roysam, E. di Tomaso, R. Tong, E.B. Brown, R.K. Jain, “Robust 3-D modeling of tumor microvasculature using superellipsoids,” *IEEE International Symposium on Biomedical Imaging: From Nano to Macro*, Arlington, Virginia, USA, pp. 185-188, 2006.

[9] J. Ripoll, V. Ntziachristos, “Imaging scattering media from a distance: Theory and applications of non-contact optical tomography,” *Mod. Phys. Lett. B*, vol. 18, pp. 1-29, 2004.

[10] F. Meyer and P. Maragos, “Multiscale Morphological Segmentations Based on Watershed, Flooding, and Eikonal PDE,” *Proc. Int’l Conf. on Scale-Space Theories in Computer Vision, Lecture Notes in Computer Science*, Springer-Verlag, vol. 1682, pp. 351-362, 1999.

[11] S.R. Arridge, “Optical tomography in medical imaging,” *Inverse Probl.*, vol. 15, pp. R41-R93, 1999.

[12] J. Ripoll, D. Yessayan, G. Zacharakis, V. Ntziachristos, “Experimental determination of photon propagation in highly absorbing and scattering media,” *J. Opt. Soc. Am. A*, vol. 22, pp. 546-551, 2005.

[13] H. Dehghani, B. Pogue, “Near infrared spectroscopic imaging: Theory,” In K.D. Paulsen, P.M. Meaney, L.C. Gilman, (editors) *Alternative Breast Imaging: Four Model-Based Approaches*, vol. 778, pp. 183-199, Netherlands, Springer, 2005.

[14] M. Guven, B. Yazici, V. Ntziachristos, “Fluorescence optical tomography with a priori information,” In F.S. Azar (editor), *Multimodal Biomedical Imaging II*, Proc. SPIE, 643107, 2007.

[15] P.P. Silvester, R.L. Ferrari, “Finite elements for electrical engineers,” *University Press*, Third Edition, Cambridge, 1996.

[16] T. Tarvainen, “Computational methods for light transport in optical tomography,” *Doctoral Dissertation*, Department of Physics, University of Kuopio, Finland, 2006.

[17] R.Y. Tsai, “A Versatile Camera Calibration Technique for High-Accuracy 3D Machine Vision Metrology Using Off-the-Shelf TV Cameras and Lenses,” *IEEE J Robot. Automat.*, vol. RA–3, pp. 323–344, 1987.

[18] O. Faugeras, “Three-Dimensional Computer Vision: a Geometric Viewpoint,” *The MIT Press*, Fourth printing, 2001.

[19] M.T. Ahmed, A.A. Farag, “Differential Methods for Nonmetric Calibration of Camera Lens Distortion,” *In Proc. IEEE Computer Society Conference on Computer Vision and Pattern Recognition*, CVPR’01, vol. 2, pp. 477-482, 2001.